Acta Oceanol. Sin., 2023, Vol. 42, No. 12, P. 39–50
https://doi.org/10.1007/s13131-023-2178-6
http://www.aosocean.com
E-mail: ocean2@hyxb.org.cn

Gravity anomalies determined from mean sea surface model data over the Gulf of Mexico

Xuyang Wei[1], Xin Liu[1]*, Zhen Li[1], Xiaotao Chang[2], Hongxin Luo[1], Chengcheng Zhu[3], Jinyun Guo[1]
[1] College of Geodesy and Geomatics, Shandong University of Science and Technology, Qingdao 266590, China
[2] Land Satellite Remote Sensing Application Center, Ministry of Natural Resources, Beijing 100048, China
[3] School of Surveying and Geo-Informatics, Shandong Jianzhu University, Jinan 250101, China

Received 19 December 2022; accepted 28 February 2023

Abstract

With the improvements in the density and quality of satellite altimetry data, a high-precision and high-resolution mean sea surface model containing abundant information regarding a marine gravity field can be calculated from long-time series multi-satellite altimeter data. Therefore, in this study, a method was proposed for determining marine gravity anomalies from a mean sea surface model. Taking the Gulf of Mexico (15°–32°N, 80°–100°W) as the study area and using a removal-recovery method, the residual gridded deflections of the vertical (DOVs) are calculated by combining the mean sea surface, mean dynamic topography, and XGM2019e_2159 geoid, and then using the inverse Vening-Meinesz method to determine the residual marine gravity anomalies from the residual gridded DOVs. Finally, residual gravity anomalies are added to the XGM2019e_2159 gravity anomalies to derive marine gravity anomaly models. In this study, the marine gravity anomalies were estimated with mean sea surface models CNES_CLS15MSS, DTU21MSS, and SDUST2020MSS and the mean dynamic topography models CNES_CLS18MDT and DTU22MDT. The accuracy of the marine gravity anomalies derived by the mean sea surface model was assessed based on ship-borne gravity data. The results show that the difference between the gravity anomalies derived by DTU21MSS and CNES_CLS18MDT and those of the ship-borne gravity data is optimal. With an increase in the distance from the coast, the difference between the gravity anomalies derived by mean sea surface models and ship-borne gravity data gradually decreases. The accuracy of the difference between the gravity anomalies derived by mean sea surface models and those from ship-borne gravity data are optimal at a depth of 3–4 km. The accuracy of the gravity anomalies derived by the mean sea surface model is high.

Key words: mean sea surface, gravity anomaly, Gulf of Mexico, inverse Vening-Meinesz formula, mean dynamic topography, satellite altimetry

Citation: Wei Xuyang, Liu Xin, Li Zhen, Chang Xiaotao, Luo Hongxin, Zhu Chengcheng, Guo Jinyun. 2023. Gravity anomalies determined from mean sea surface model data over the Gulf of Mexico. Acta Oceanologica Sinica, 42(12): 39–50, doi: 10.1007/s13131-023-2178-6

1 Introduction

Marine gravity is of great significance in geodesy, marine geophysics, aerospace technology research and military applications. With the development of satellite altimetry technology, satellite altimetry data has been the primary data source for marine gravity derivations (Andersen et al., 2010; Sandwell et al., 2014; Li et al., 2022a; Zhu et al., 2022). At present, continuous high-precision sea surface altimetry data with a duration of several decades can be obtained. The improvements in the data accuracy and abundant high-frequency information (Chelton et al., 1989) contained in satellite altimetry data provide effective data support for the study of global sea levels and their variations (Stanev and Peneva, 2001; Jin and Li, 2012; Li et al., 2022b), marine gravity anomalies (Zhu et al., 2019), mean sea surfaces (Yuan et al., 2021), seafloor topographies (Hwang and Chang, 2014; Yang et al., 2018), ocean lithospheres (Gozzard et al., 2019) and ocean circulations (Guo et al., 2010; Zaron, 2019).

With the abundance of altimetry data and the improvement of its quality, domestic and foreign scholars have used satellite altimetry data to invert the derivations of marine gravity fields (Sandwell et al., 2013; Zhu et al., 2022; Guo et al., 2022). The methods for deriving marine gravity anomalies using satellite altimetry data mainly include the least square collocation (LSC) method (Rapp, 1979; Smith, 1974), inverse Stokes formula (Gopalapillai, 1974; Liu et al., 2016), Laplace equation (Sandwell and Smith, 1997), and inverse Vening-Meinesz (IVM) formula (Hwang, 1998). Although the existing methods for deriving marine gravity anomalies can obtain high accuracy, they still have certain limitations. Using the LSC method to invert marine gravity anomalies requires determining the variance and covariance matrix between signals in the region. However, it is not easy to determine the variance and covariance matrix between signals in the global scope, so the LSC method is only applicable in local sea areas at present. It is necessary to obtain a high-precision and high-resolution mean dynamic topography (MDT) model when using the inverse Stokes formula to invert marine gravity anomalies, but the spatial resolution of MDT models requires further improvement (Wan and Yu, 2013). Deriving marine gravity anomalies using the Laplace equation requires distinguishing disturbing gravity from gravity anomaly information. When using

---

Foundation item: The National Natural Science Foundation of China under contract Nos 42274006, 42174041 and 41774001; the Research Fund of University of Science and Technology under contract No. 2014TDJH101.

*Corresponding author, E-mail: xinliu1969@126.com

the IVM formula to invert marine gravity anomalies, determining the appropriate kernel function is key, and the inner band effect should also be considered. The above methods for the derivation of marine gravity anomalies use data concerning sea surface heights, geoids, and vertical deviations from satellite altimetry data, but there are presently few related research studies on the derivation of marine gravity anomalies using mean sea surface (MSS) model data.

The MSS is a relatively stable sea surface height and one of the important parameters in geodesy and physical oceanography (Andersen et al., 2005). It can be used as a reference datum for a national elevation datum in geodesy, a reference datum for ocean vertical datum in oceanography, and in research on ocean circulation and mesoscale vortex detection, sea surface height change analysis, geoid fluctuation determination, and crustal deformation detection (Fu and Cazenave, 2001). With the development of satellite altimetry technology, a greater amount of time series, high-precision, and high-resolution sea surface height data can be obtained. Therefore, multi-source satellite altimetry data can be used to establish a high-precision and high-resolution global and regional MSS model for estimating marine gravity anomalies.

The Gulf of Mexico, an ocean between the United States and Mexico, is located in the area where the North American plate, Caribbean plate, and Cox plate interact with each other, making the Gulf of Mexico present unique geological structural characteristics. Moreover, there are many oil-bearing basins in the Gulf of Mexico, which is also a hot spot for oil and gas exploration and development. Accurate derivation of the gravity anomalies in the Gulf of Mexico is beneficial to the study of the Gulf of Mexico fault (Fairhead et al., 2001), oceanic crust distributions, and the geological changes caused by oil and gas exploration.

In this study, gravity anomalies in the Gulf of Mexico are inverted by the IVM formula using an MSS model and MDT model. The MSS models CNES_CLS15MSS, DTU21MSS, and SDUST 2020MSS, and the MDT models CNES_CLS18MDT and DTU22 MDT are selected for estimating gravity anomalies in the Gulf of Mexico, and the accuracy of the marine gravity anomalies derived from the MSS model are assessed based on ship-borne gravity data.

2 Study region and data

2.1 *Study region*

In this study, the Gulf of Mexico is selected as the study area; its range is 15°–32°N, 80°–100°W. There are many alluvial fan fold belts in the coastal part of the study area, with the Florida Islands, Cayman Islands, Youth Island, and other islands distributed in the area. Special seafloor topography such as the Mexico Basin, Yucatan Basin, Cayman Ridge, Siegsby Trench, and Cayman Trench is also included in the study area (Ismael, 2014). The lowest depth in the study area is located in the Cayman Trench, which reaches 6 000 m, as shown in Fig. 1.

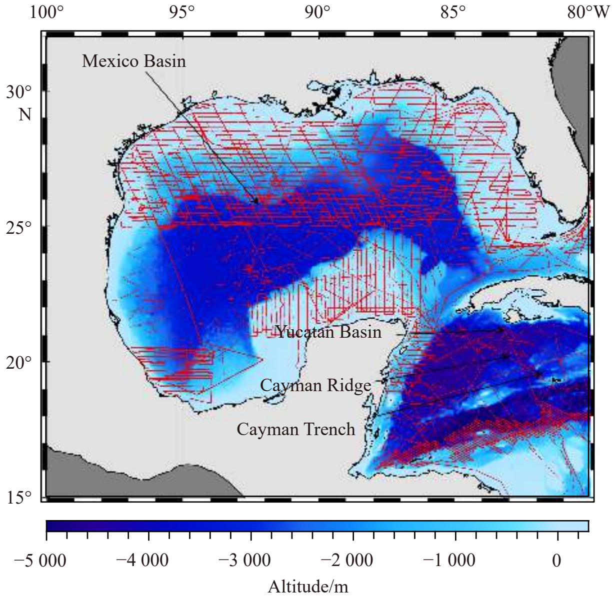

Fig. 1. Study area and ship-borne gravity trace distribution. The thick solid red line is ship-borne gravity trace; the light gray area is land; the dark gray area corresponds to the marine regions that have been excluded from consideration or inclusion in this study.

2.2 *Mean sea surface model*

In this study, the MSS model CNES_CLS15MSS (Pujol et al., 2018) (download address: https://www.aviso.altimetry.fr/en/index.php?id=1615) published by Centre National d 'Etudes Spatiales (CNES) is adopted. The global coverage is 80°S–84°N, the grid resolution is 1′ × 1′, and the reference period is from 1993 to 2012. The establishment of the model integrates the data of seven altimetry satellites, including Topex/Poseidon (T/P), Jason-1, Jason-2, ERS-2, Envisat, GeoSat follow-on (GFO), and Cryosat-2. In addition, the local least squares collocation method is used in the process of establishing the model, and the noise of the altimeter satellites and deviation along the orbit are considered to improve the data accuracy and establish a high-precision and high-resolution global MSS model.

The MSS model DTU21MSS (Andersen et al., 2021) (download address: https://ftp.space.dtu.dk/pub/DTU21/) is published by the Technical University of Denmark (DTU). The global coverage is 90°S–90°N, the grid resolution is 1′ × 1′, and the reference period is from 1993 to 2012. The establishment of this model integrates the altimeter satellite data of T/P, Jason-1, Jason-2, ERS-1, ERS-2, EN-VISAT, ICESat, Geosat, GFO, CryoSat-2, and Sentinel-3A. The 5-year Sentinel-3A and improved 10-year Cryosat-2 low-resolution model, synthetic aperture radar (SAR) model, and SAR interference mode model data are used to establish a high-precision and high-resolution global MSS model.

The MSS model SDUST2020MSS (Yuan et al., 2023) (download address: https://zenodo.org/record/6555990) was published by Shandong University of Science and Technology (SDUST). The global coverage is 80°S–84°N, the grid resolution is 1′ × 1′, and the reference period is from 1993 to 2019. The establishment of the model integrates the altimeter satellite data of T/P, Jason-1, Jason-2, Jason-3, ERS-1, ERS-2, GFO, Envisat, SARAL, HY-2A, Sentinel-3A, and Cryosat-2. Among the used multi-source satellite altimetry data, the HY-2A, Jason-3, and Sentinel-3A satellite altimetry data are used for the first time to establish a high-precision and high-resolution global MSS model. Details are shown in Table 1.

2.3 *Mean dynamic topography model*

This study considers CNES_CLS18MDT (Mulet et al., 2021) (download address: https://www.aviso.altimetry.fr/en/data/products/auxiliary-products/mdt), a global MDT model with a grid resolution of 7.5′ × 7.5′ published by CNES. The model is calculated based on the geoid model GOCO05S and CNES_CLS15MSS. The geoid model GOCO05S uses complete “Gravity Field and Steady-State Ocean Circulation Explorer” mission data and 10.5 years of “Gravity Recovery and Climate Experiment”

Table 1. Basic information of global mean sea surface models

Mean sea surface model	Grid size	Coverage area	Altimeter data
CNES_CLS15MSS	1′× 1′	80°S–84°N	T/P + J1 + J2 + E2 + En + GFO + C2
DTU21MSS	1′× 1′	90°S–90°N	T/P + J1 + J2 + E1 + E2 + En + Ic + Ge + GFO + C2 + S3A
SDUST2020MSS	1′× 1′	80°S–84°N	T/P + J1 + J2 + J3 + E1 + E2 + GFO + En + H2 + C2 + Al + S3A

Note: T/P, Topex/Poseidon; J1, Jason-1; J2, Jason-2; J3, Jason-3; E1, ERS-1; E2, ERS-2; En, Envisat; GFO, GeoSat follow-on; Ic, Icesat; Ge, Geosat; H2, HY-2A; C2, Cryosat-2; Al, Saral/Altika; S3A, Sentinel-3A.

mission data. CNES_CLS18MDT also comprehensively uses 25-year altimetry data, temperature data, salinity data, buoy data, and hydrological model data.

The global MDT model DTU22MDT (download address: https://ftp.space.dtu.dk/pub/DTU22/MDT/) was published by DTU and has a grid resolution of 7.5′ × 7.5′. The model is calculated based on the geoid model XGM2019e and DTU21MSS. DTU21MSS is calculated using multi-task altimeter data representing a 20-year average (1993–2012).

2.4 *Seafloor topography model*

This study uses the global seafloor topography model SIO topo_23.1 (Sandwell and Smith, 1997) (download address: https://topex.ucsd.edu/pub/global_topo_1min) with a grid resolution of 1′ × 1′, as published by Scripps Institute of Oceanography (SIO), University of California, San Diego, USA in 2021. It has a global coverage of 80°N–80°S. SIO topo_23.1 is used for the land topography data, coastline data, and water depth-terrain comprehensive data. It is also used to assess the accuracy of the MSS model in the derivation of marine gravity anomalies at different seafloor topographies.

2.5 *Reference gravity field model*

In this study, the removal-recovery method is used for the derivation of gravity anomalies, and a high-precision and high-resolution reference gravity field model is needed; thus, the gravity anomaly model XGM2019e_2159 is selected. The model is a 1′×1′ gravity anomalies grid model calculated from the gravity anomaly model XGM2019e by the International Center for Global Earth Models (ICGEM) (download address: http://icgem.gfz-potsdam.de/calcgrid) and was released in 2019. XGM2019e is a combined global gravity field model. The data sources of this model mainly include the gravity field model GOCO06s, ground gravity grid data compiled by the NGA, and the augmentation dataset consisting of gravity anomalies derived from altimetry over the oceans and topography over the continents. Generally speaking, the XGM2019e model has better performance for the ocean and is independent of the existing high-resolution gravity field model (Mulet et al., 2021). The order of the spherical harmonic coefficient of this model can be expanded to 5 399, and the order of the model used herein can be expanded to 2 159 (Zingerle et al., 2020) (i.e., one of the latest gravity field models at present).

2.6 *Ship-borne gravity data*

The ship-borne gravity data for this study is provided by the National Centers for Environmental Information (NCEI) under the National Oceanic and Atmospheric Administration of the United States. It is a global aggregate of measured marine gravity datasets as measured by different departments and instruments. There are 35 ship-borne routes in the study area, and the period is from 1961 to 1995. With improvements in navigation accuracy, the accuracy of the marine gravity field information obtained by ship-borne gravity measurements is gradually improving, and its measurement theories and methods are mature. Moreover, the operational flow and data processing methods are gradually improving. A ship-borne survey is less affected by the seafloor topography, and its offshore measurement accuracy is high. It is usually used to measure regional gravity anomalies and is also used to check the derivations of gravity anomalies using satellite altimetry data. In addition, the satellite altimetry data can be fused to improve the accuracy of the marine gravity field. The distribution of the NCEI ship-borne gravity trace in the study area is shown in Fig. 1.

Because each ship-borne route is measured by different organizations in different periods using different instruments, there are many long-wave errors in the ship-borne data. These are mainly caused by drifts of gravimeters, differences in reference fields, and incorrect and/or horizontal connections of reference stations (Hwang and Parsons, 1995).

The uncertainty regarding an ellipsoidal system and error caused by the drift of the gravimeter can be corrected by using a quadratic polynomial when measuring the ship sailing at a uniform speed along the route, as follows:

$$\Delta g_{\text{ship}} = x_0 + x_1 \Delta t + x_2 \Delta t^2, \tag{1}$$

where Δg_{ship} is the corrected value of the ship-borne gravity; Δt is the time interval between the observation time and starting time of the shipping route; x_0, x_1 and x_2 are parameters to be fitted; x_0 represents the standard deviation, and x_1 and x_2 represent the total influences of different error sources as estimated by the least squares method (Zhu et al., 2021).

The quadratic polynomial is used to calculate the gravity correction value of each ship-borne point, and the corresponding ship-borne point is corrected. The information regarding the difference between the ship-borne gravity data before and after correction and the gravity anomaly of the XGM2019e_2159 model is counted. It can be seen from Table 2 that before and after the correction of the ship-borne gravity data using the quadratic polynomial, the difference values of maximum (Max), minmum (Min), mean, standard deviation (STD), and root mean square (RMS) of the ship-borne gravity anomalies and XGM2019e_2159 model gravity anomalies decrease significantly, and the accuracy im-

Table 2. Statistics of the difference between the ship-borne gravity data and XGM2019e_2159 gravity anomaly model

State	Data number	Difference value				
		Max/mGal	Min/mGal	Mean/mGal	STD/mGal	RMS/mGal
Before correction	266 361	181.11	–90.51	0.53	7.10	7.12
After correction	251 023	43.63	–40.73	0.04	3.98	3.98
After excluding routes[1)]	249 908	38.34	–36.31	0.04	3.91	3.91

Note: [1)] Excluded routes are routes v2103 and u271gm.

proves significantly. However, the Max of the difference remains excessively large, indicating that gross errors remain in the ship-borne data. The accuracy of each ship-borne route before and after correction is therefore analyzed. In the experiment, the STD of the difference between the observed value of each route and that from the model of the earth gravity field XGM2019e_2159 are counted and recorded as σ_i ($i = 1, 2, 3, \cdots, 35$). Then, the STD is calculated of the difference between the observed values of all routes in the area and those of the XGM2019e_2159 model and recorded as σ_{all}. According to the principle of 3σ, routes with σ_i greater than three times σ_{all} are eliminated. Table 2 provides accurate information on the ship-borne data after excluding abnormal routes, and Table 3 provides specific information regarding abnormal routes.

According to Table 2, after the ship-borne gravity data is corrected using a quadratic polynomial, the RMS of the gravity difference with the XGM2019e_2159 model is reduced to 3.98 mGal before correction. When the ship-borne routes listed in Table 3 are eliminated, the RMS of the gravity difference between the ship-borne gravity data and XGM2019e_2159 model is reduced to 3.91 mGal, and the accuracy is evidently improved.

3 Methodology

3.1 *Residual vertical deviations calculation*

The cubic spline interpolation method is used to interpolate the grid data of CNES_CLS18MDT and DTU22MDT with a grid of 7.5′ × 7.5′ into a grid data with a grid of 1′ × 1′. With the removal-recovery method, the residual geoid data N_{res} can be obtained by deducting the influence of the interpolated MDT and reference field XGM2019e_2159 geoid N_{ref} from MSS, as follows:

$$N_{\text{res}} = \text{MSS} - \text{MDT} - N_{\text{ref}}. \tag{2}$$

The equations for calculating the meridian and prime vertical components of the residual vertical deviation of the grid points are as follows:

$$\xi_{\text{res}_\text{A}} = \tan\alpha = \frac{N_{\text{re}}}{\text{s}_\text{P} - N_{\text{res}_\text{A}}} d_{y,\text{AP}} = \frac{\Delta N_{\text{res}_\text{AP}}}{d_{y,\text{AP}}}, \tag{3}$$

$$\eta_{\text{res}_\text{A}} = \tan\beta = \frac{N_{\text{res}_\text{Q}} - N_{\text{res}_\text{A}}}{d_{x,\text{AQ}}} = \frac{\Delta N_{\text{res}_\text{AQ}}}{d_{x,\text{AQ}}}. \tag{4}$$

The relatively small area near the grid point can be treated as a plane, where $\xi_{\text{res}_\text{A}}$ is the meridian component of the residual vertical deviation of the grid point and $\eta_{\text{res}_\text{A}}$ is the prime vertical component of the residual vertical deviation of the grid point. N_{res_A}, N_{res_P}, and N_{res_Q} are the residual geoids of A, P, and Q, respectively. $d_{y,\text{AP}}$ is the spherical distance between A and P in the north-south direction and $\text{d}_{x,\text{AQ}}$ is the spherical distance between A and Q in the east-west direction, as shown in Fig. 2.

3.2 *Gravity anomaly derivation by inverse Vening-Meinesz (IVM)*

The formula for calculating the residual gravity anomaly Δg_{res} using the IVM formula (Sandwell and Smith, 1997; Hwang, 1998; Sandwell et al., 2013) from the gridding residual vertical deviation is as follows:

$$\Delta g_{\text{res}}(\text{A}) = \frac{\gamma_0}{4\pi} \iint_\sigma H'(\psi_{\text{AQ}})(\xi_{\text{res}_\text{Q}} \cos\alpha_{\text{QA}} + \eta_{\text{res}_\text{Q}} \sin\alpha_{\text{QA}}) \text{d}\sigma_\text{Q}, \tag{5}$$

where A is the fixed point, Q is the flowing point, and $\gamma_0 = \frac{\text{GM}}{R^2}$ is the normal gravity at point A (GM is the gravitational constant of the earth, and R is the average radius of the earth). $\xi_{\text{res}_\text{Q}}$ and $\eta_{\text{res}_\text{Q}}$ are the meridian and prime vertical components of the residual vertical deviation at the flow point Q, respectively, and a_{QA} is the azimuth angle from point Q to point A. $H'(\psi_{\text{AQ}})$ is the derivative of the kernel function of ψ_{AQ}, and is calculated as follows:

$$H'(\psi_{\text{AQ}}) = \frac{\cos\dfrac{\psi_{\text{AQ}}}{2}}{2\sin^2\dfrac{\psi_{\text{AQ}}}{2}} + \frac{\cos\dfrac{\psi_{\text{AQ}}}{2}\left(3 + 2\sin\dfrac{\psi_{\text{AQ}}}{2}\right)}{2\sin\dfrac{\psi_{\text{AQ}}}{2}\left(1 + \sin\dfrac{\psi_{\text{AQ}}}{2}\right)}, \tag{6}$$

where ψ_{AQ} is the spherical distance between points A and Q.

When predicting the gravity anomaly on the grid point, when the spherical distance ψ is 0, equation $H'(\psi)$ will be singular. Therefore, the influence of the innermost band must be considered when using the IVM method. The remaining gravity anomaly Δg_{inzone} in the innermost zone is calculated as follows:

$$\Delta g_{\text{inzone}} = \frac{1}{2} s_0 \gamma_0 (\xi_{\text{res}_x} + \eta_{\text{res}_y}), \tag{7}$$

where ξ_{res_x} is the north derivative of the meridional component of the residual vertical deviation, η_{res_y} is the east derivative of the

Table 3. Statistical information of abnormal ship-borne routes

Route	Data number	Time	STD before correction/mGal	STD after correction/mGal
v2103	680	1965/03/01–1965/03/10	15.76	15.03
u271gm	443	1971/06/27–1971/07/08	21.95	21.95

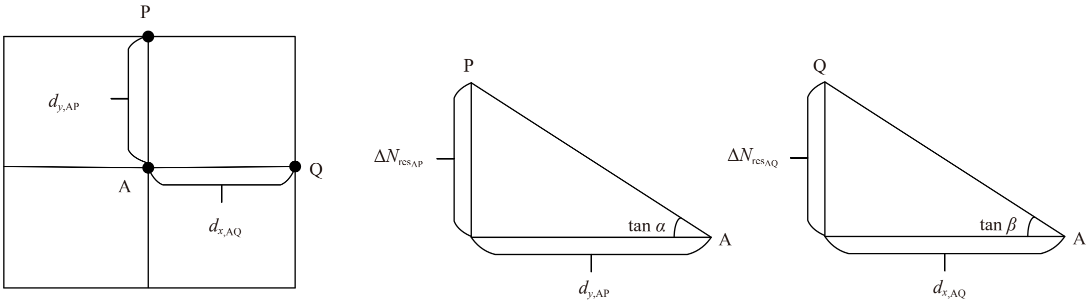

Fig. 2. Calculation diagram of the residual gridded deflections of the vertical (DOVs).

prime vertical component of the residual vertical deviation, and $s_0=\sqrt{\frac{\Delta x\Delta y}{\pi}}$ is the size of the innermost zone. Δx and Δy are the spacing sizes of the gridded DOVs in the east and north directions, respectively.

Finally, Eqs (5) and (7) are used to calculate the residual gravity anomaly $\Delta g_{\rm res}$ and the inner ring residual gravity anomaly $\Delta g_{\rm inzone}$, respectively, and the gravity anomaly $\Delta g_{\rm ref}$ of the XGM2019e_2159 reference field is restored. The final gravity anomaly Δg is the sum of them, as follows:

$$\Delta g=\Delta g_{\rm res}+\Delta g_{\rm inzone}+\Delta g_{\rm ref}. \tag{8}$$

The derivation of the gravity anomalies in the Gulf of Mexico using the above methodology is shown in Fig. 3.

4 Results and analysis

4.1 *Marine gravity anomalies*

In this study, using CNES_CLS15MSS, DTU21MSS, and SDUST2020MSS combined with CNES_CLS18MDT and DTU22MDT, the gravity anomalies models of the Gulf of Mexico grid with the size of 1′ × 1′ are inverted using IVM method (see Fig. 4). Grav-1 is a gravity anomaly model using CNES_CLS15MSS and CNES_CLS18MDT inversion. Grav-2 is a gravity anomaly model using CNES_CLS15MSS and DTU22MDT inversion. Grav-3 is a gravity anomaly model using DTU21MSS and CNES_CLS18MDT inversion. Grav-4 is a gravity anomaly model using DTU21MSS and DTU22MDT inversion. Grav-5 is a gravity anomaly model using SDUST2020MSS and CNES_CLS18MDT inversion. Grav-6 is a gravity anomaly model using SDUST2020MSS and DTU22MDT inversion.

According to Figs 1 and 4, there are strong similarities among Grav-1, Grav-2, Grav-3, Grav-4, Grav-5, and Grav-6, that is, the trend of the gravity anomaly changes from west to east or from south to north is similar to that of seafloor topography and water depth in this area. The abnormal gravity change is gently in sea areas with gentle topography and no islands, but it is very severe in sea areas with complex seafloor topographies or islands. Taking Fig. 4a as an example, the maximum value of the gravity an-

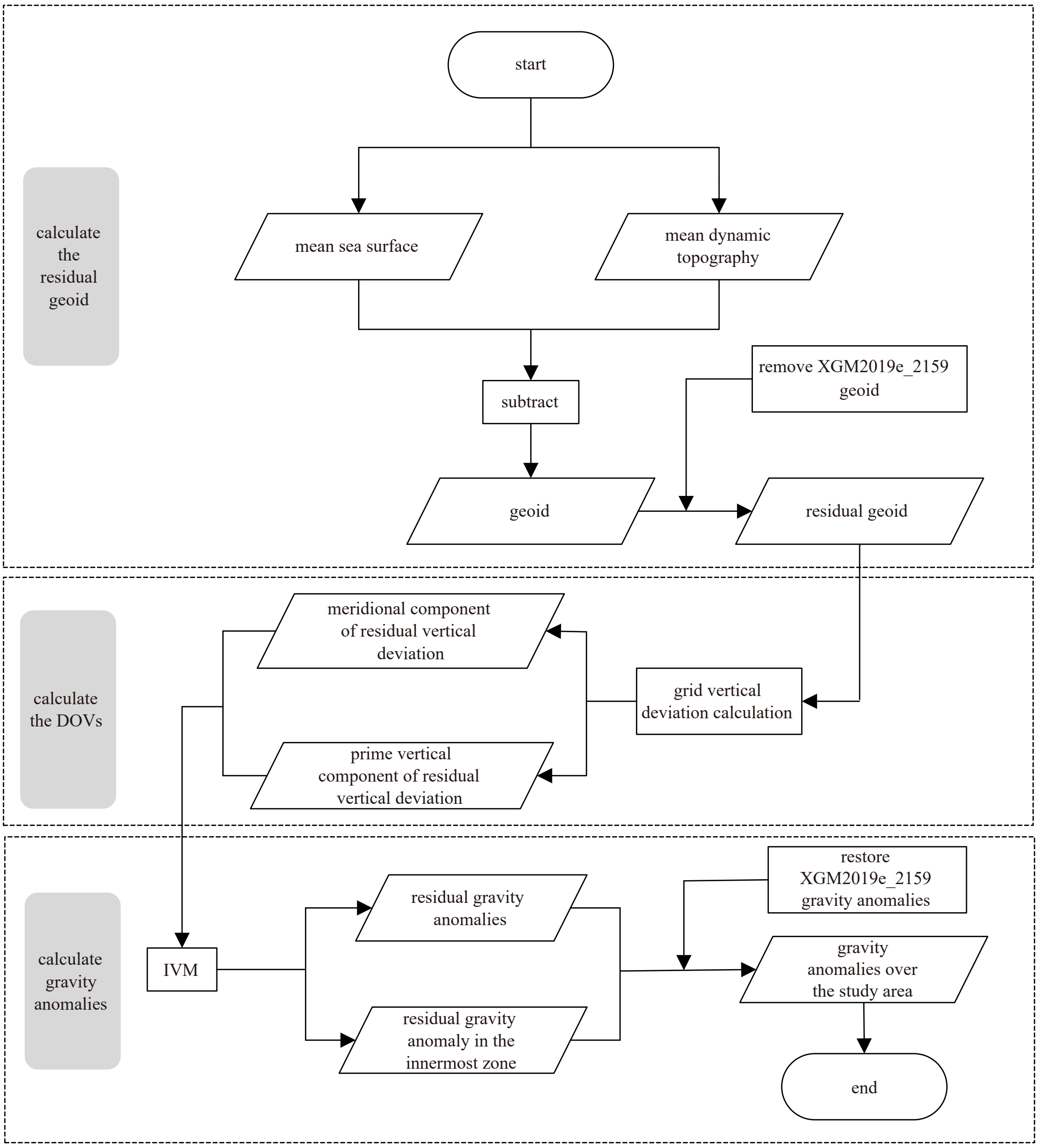

Fig. 3. Flowchart of data processing of deriving gravity anomalies using the mean sea surface model.

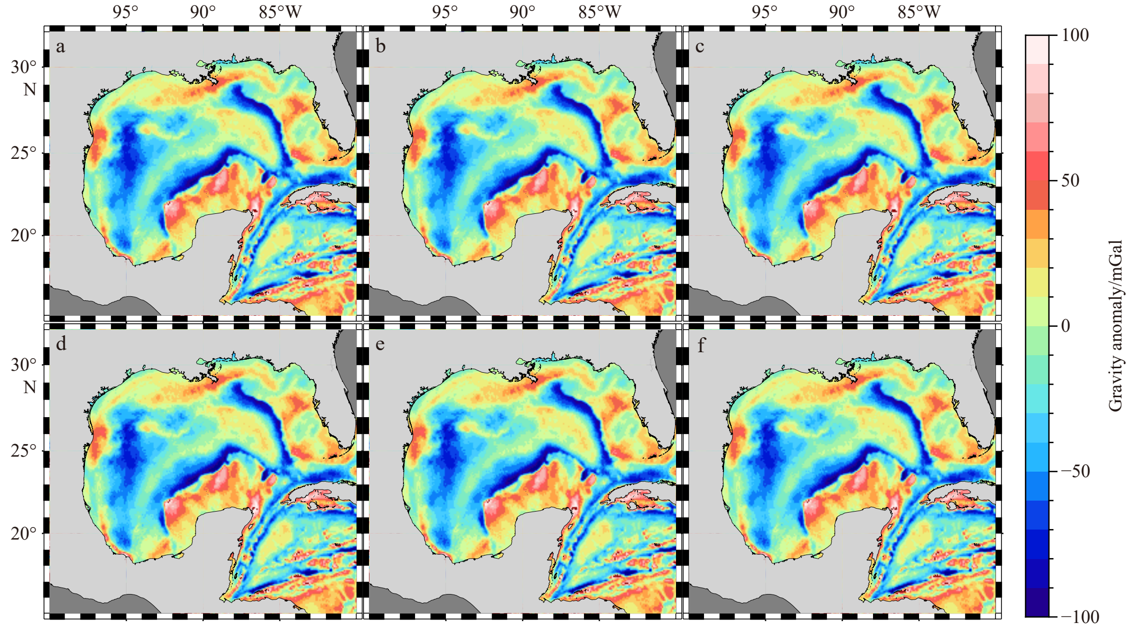

Fig. 4. Gravity anomalies derived from mean sea surface models: Grav-1 (a); Grav-2 (b); Grav-3 (c); Grav-4 (d); Grav-5 (e); Grav-6 (f).

omaly at 96°W ridge reaches 315 mGal, and the minimum value of gravity anomaly near the Cayman Trench reaches –148 mGal.

Figures 4 and 6 show that the derived gravity anomaly models from the MSS models are similar and that differences among the six gravity anomaly models are mostly on the order of ±1 mGal. To verify the accuracy differences of the six gravity anomaly models, the spatial distribution maps of gravity anomalies differences among the six models of Grav-1, Grav-2, Grav-3, Grav-4, Grav-5 and Grav-6 were drawn (see Fig. 5). According to Fig. 5, these differences are mainly concentrated in the coastal and eastern part of the Gulf of Mexico (23°–28°N and 80°–85°W). This is because the establishment of CNES_CLS15MSS, DTU21MSS and SDUST2020MSS integrated different altimeter satellite data. The difference shown in Figs 5a, j and o is small. This shows that the same MSS model and different MDT models are used to invert the marine gravity anomaly, and the differences between different MDT models have little influence on the derived marine gravity anomalies.

4.2 *Accuracy evaluation*

The ship-borne gravity data provides an effective way to evaluate the accuracy of the marine gravity field model. A total of 266 361 ship-borne gravity data elements in the study area (15°–32°N, 80°–100°W) are selected. Owing to the sea conditions, instrument levels, and observation errors, the ship-borne gravity data inevitably includes gross errors. All of the routes in the study area are corrected by using the quadratic polynomial to eliminate the abnormal values. This effectively improves the evaluation

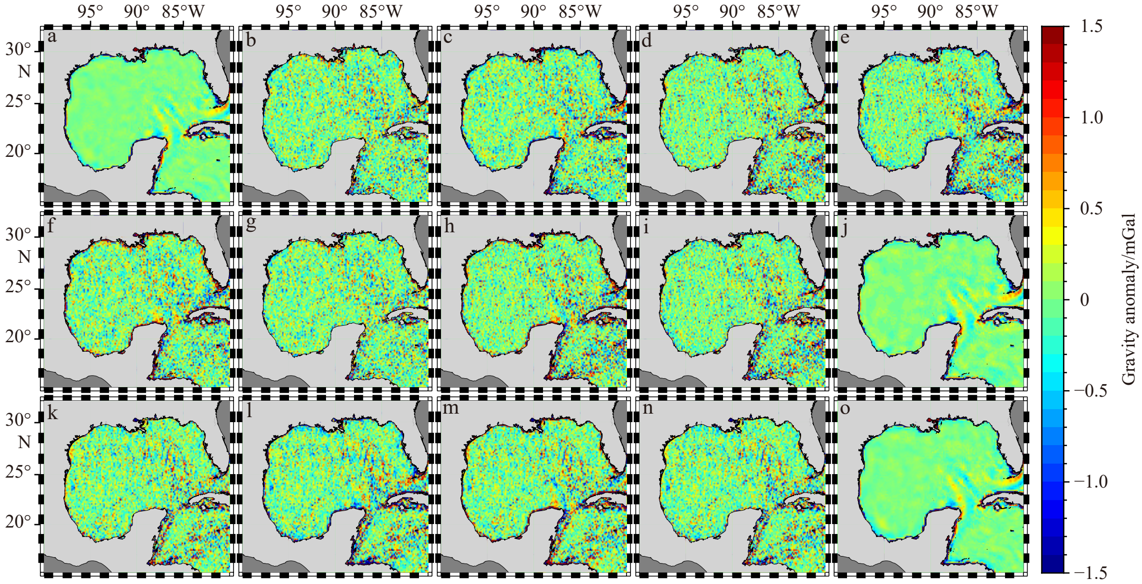

Fig. 5. Differences among six marine gravity anomaly models. a. Grav-1 – Grav-2; b. Grav-1 – Grav-3; c. Grav-1 – Grav-4; d. Grav-1 – Grav-5; e. Grav-1 – Grav-6; f. Grav-2 – Grav-3; g. Grav-2 – Grav-4; h. Grav-2 – Grav-5; i. Grav-2 – Grav-6; j. Grav-3 – Grav-4; k. Grav-3 – Grav-5; l. Grav-3 – Grav-6; m. Grav-4 – Grav-5; n. Grav-4 – Grav-6; o. Grav-5 – Grav-6.

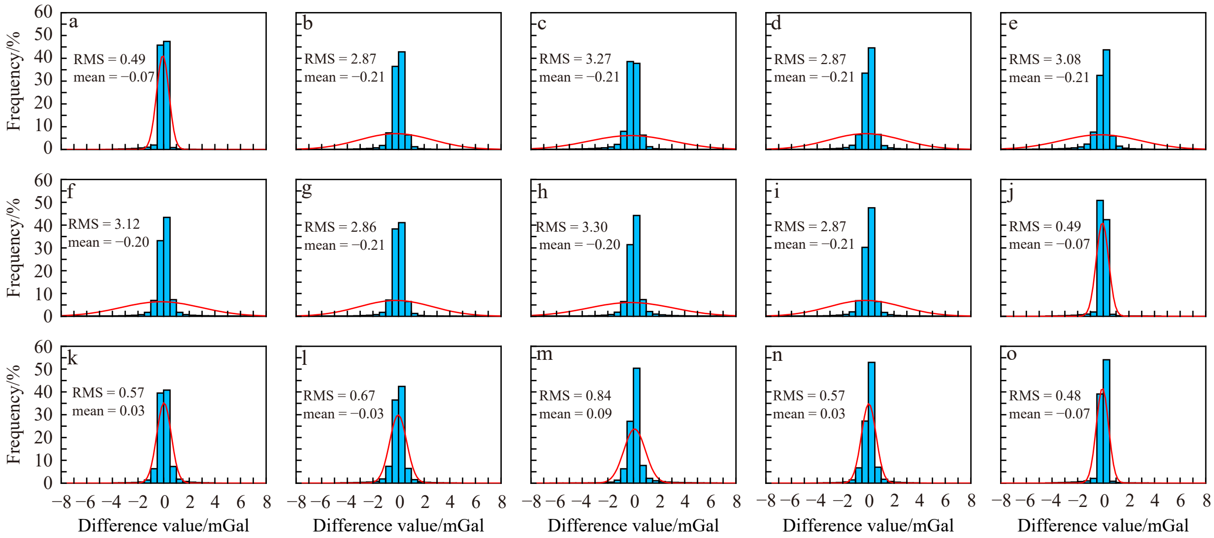

Fig. 6. Histogram distribution of differences among the six marine gravity anomaly models. The red line is the normal distribution curve. a. Grav-1 – Grav-2; b. Grav-1 – Grav-3; c. Grav-1 – Grav-4; d. Grav-1 – Grav-5; e. Grav-1 – Grav-6; f. Grav-2 – Grav-3; g. Grav-2 – Grav-4; h. Grav-2 – Grav-5; i. Grav-2 – Grav-6; j. Grav-3 – Grav-4; k. Grav-3 – Grav-5; l. Grav-3 – Grav-6; m. Grav-4 – Grav-5; n. Grav-4 – Grav-6; o. Grav-5 – Grav-6.

accuracy of the ship-borne gravity data under the condition that the rejection rate is less than 2% of the observed values (Guo et al., 2022). The Max, Min, mean, STD, and RMS values of the differences between the gravity field models of Grav-1, Grav-2, Grav-3, Grav-4, Grav-5, XGM2019e_2159, and the ship-borne gravity data are shown in Table 4.

According to the statistical results of the difference between Grav-1, Grav-2, Grav-3, Grav-4, Grav-5, Grav-6 and the ship-borne gravity data in Table 4, the accuracy of the differences between XGM2019e_2159 and the ship-borne gravity data is effectively improved. The accuracy of the difference between Grav-3 and the ship-borne gravity data is the best with an RMS of 3.66 mGal, whereas that between Grav-5 and the ship-borne gravity data is the worst with an RMS of 3.77 mGal.

Figure 7 shows the vertical distribution of the differences between Grav-1, Grav-2, Grav-3, Grav-4, Grav-5, and Grav-6, and the ship-borne gravity data. Statistically, the differences between the six marine gravity anomaly models and ship-borne gravity data are very similar, and the differences between them meet the characteristics of normal distributions. According to the statistics, the differences between Grav-1, Grav-2, Grav-3, Grav-4, Grav-5, and Grav-6 and the ship-borne gravity data are 97.66%, 97.66%, 97.81%, 97.81%, 97.54%, and 97.54% within ±10 mGal, respectively. The percentages of points in the range where the difference between Grav-1, Grav-2, Grav-3, Grav-4, Grav-5, and Grav-6 and the ship-borne gravity data is greater than ±10 mGal are 2.34%, 2.34%, 2.19%, 2.19%, 2.46%, and 2.46%, respectively. It can be seen that the differences between Grav-3 and Grav-4 and the ship-borne gravity data are more concentrated, and can better reflect the abnormal information of the marine gravity.

To analyze the relationships between the accuracy of Grav-1, Grav-2, Grav-3, Grav-4, Grav-5, and Grav-6 and the distance from the coastline, the differences between the six marine gravity anomaly models and the ship-borne gravity data at different distances from the coastline are counted. The specific statistical results are shown in Table 5.

It can be seen from Table 5 that the difference between the six marine gravity anomaly models and ship-borne gravity data decreases with the increase of the distance from the coastline. The RMS reduction rate of the difference between the gravity anomaly retrieved from 0–20 km from the coastline and ship-borne gravity data is evident. This is because the closer to the coast, the greater the impact on the satellite echo waveform, and the lower the derivation accuracy. However, the RMS reduction rate of the difference between the gravity anomaly retrieved 20–50 km away from the coastline and ship-borne gravity data is lower. This is because the satellite echo waveform is gradually decreasing owing to the influence of the coastal shallow water area, and the accuracy is not improved. Therefore, in the far sea, there is little difference between the six marine gravity anomaly models and the ship-borne gravity data.

It can be seen from Figs 1 and 4 that the gravity anomaly derivation changes with changes in the seawater depth. Therefore, Grav-1, Grav-2, Grav-3, Grav-4, Grav-5, and Grav-6 are selected to compare the differences between the derivation gravity anomalies at different depths and the ship-borne gravity data. The stat-

Table 4. Statistics of the difference between marine gravity field model and the ship-borne gravity data

Model	Max/mGal	Min/mGal	Mean/mGal	STD/mGal	RMS/mGal
Grav-1	38.53	–36.17	0.07	3.71	3.71
Grav-2	38.49	–37.64	0.09	3.72	3.72
Grav-3	39.31	–35.81	0.07	3.66	3.66
Grav-4	39.30	–35.79	0.08	3.67	3.67
Grav-5	38.19	–35.97	0.07	3.77	3.77
Grav-6	38.20	–35.94	0.10	3.76	3.76
XGM2019e_2159	38.34	–36.31	0.04	3.91	3.91

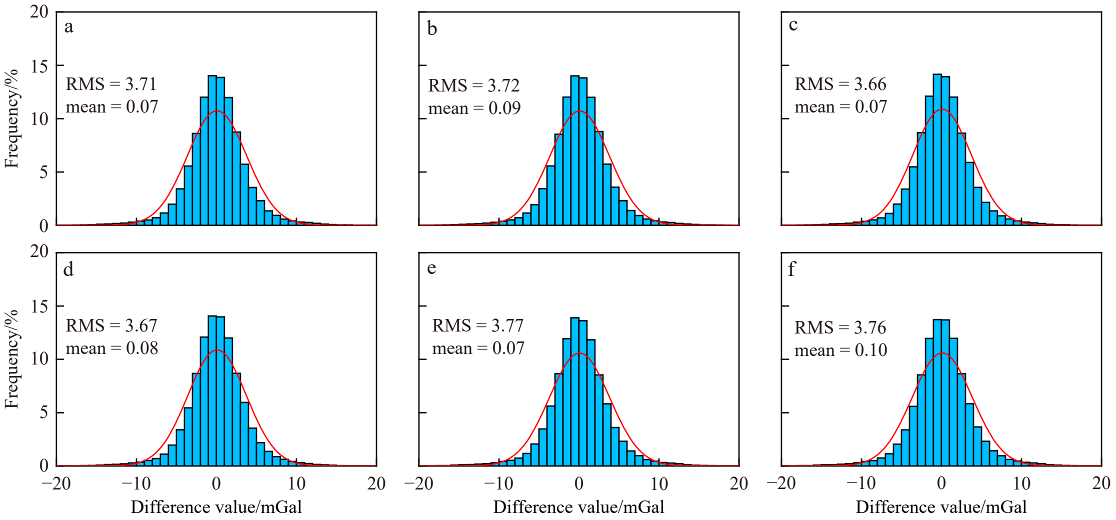

Fig. 7. Histogram distribution of difference between marine gravity anomaly models and the ship-borne gravity data. a. Grav-1 – NCEI; b. Grav-2 – NCEI; c. Grav-3 – NCEI; d. Grav-4 – NCEI; e. Grav-5 – NCEI; f. Grav-6 – NCEI. The red line is the normal distribution curve.

Table 5. Statistics of the difference between marine gravity anomaly models and the ship-borne gravity data at different distances from coastline

Model	Distance from coastline/km	Data number	Max/mGal	Min/mGal	Mean/mGal	STD/mGal	RMS/mGal
Grav-1	>0	249 908	38.53	−36.17	0.07	3.71	3.71
	>10	247 401	38.53	−36.17	0.07	3.67	3.67
	>20	241 044	38.53	−36.17	0.07	3.59	3.59
	>30	232 606	38.53	−36.17	0.08	3.53	3.54
	>40	223 320	38.53	−36.17	0.09	3.50	3.50
	>50	214 231	37.81	−36.17	0.11	3.48	3.48
Grav-2	>0	249 908	38.49	−37.64	0.09	3.72	3.72
	>10	247 401	38.49	−36.16	0.08	3.67	3.67
	>20	241 044	38.49	−36.16	0.07	3.59	3.59
	>30	232 606	38.49	−36.16	0.08	3.54	3.54
	>40	223 320	38.49	−36.16	0.09	3.50	3.51
	>50	214 231	37.88	−36.16	0.11	3.48	3.49
Grav–3	>0	249 908	39.31	−35.81	0.07	3.66	3.66
	>10	247 401	39.31	−35.81	0.07	3.63	3.63
	>20	241 044	39.31	−35.81	0.07	3.56	3.56
	>30	232 606	39.31	−35.81	0.07	3.50	3.50
	>40	223 320	39.31	−35.81	0.09	3.47	3.47
	>50	214 231	37.91	−35.81	0.10	3.45	3.45
Grav-4	>0	249 908	39.30	−35.79	0.08	3.67	3.67
	>10	247 401	39.30	−35.79	0.07	3.63	3.63
	>20	241 044	39.30	−35.79	0.07	3.56	3.56
	>30	232 606	39.30	−35.79	0.07	3.51	3.51
	>40	223 320	39.30	−35.79	0.09	3.48	3.48
	>50	214 231	37.99	−35.79	0.10	3.46	3.46
Grav-5	>0	249 908	38.19	−35.97	0.07	3.77	3.77
	>10	247 401	38.19	−35.97	0.06	3.74	3.74
	>20	241 044	38.19	−35.97	0.07	3.66	3.66
	>30	232 606	38.19	−35.97	0.08	3.60	3.60
	>40	223 320	38.19	−35.97	0.09	3.57	3.57
	>50	214 231	38.19	−35.97	0.10	3.55	3.55
Grav-6	>0	249 908	38.20	−35.94	0.10	3.76	3.76
	>10	247 401	38.20	−35.94	0.09	3.74	3.74
	>20	241 044	38.20	−35.94	0.08	3.66	3.66
	>30	232 606	38.20	−35.94	0.09	3.60	3.61
	>40	223 320	38.20	−35.94	0.10	3.57	3.57
	>50	214 231	38.20	−35.94	0.11	3.55	3.55

istical results are shown in Table 6.

It can be seen from Table 6 that when the depth is 3–4 km, the accuracy of the six marine gravity anomaly models and ship-borne gravity data is the best. This is because these points are mostly distributed near the sea basin, where the seafloor topography changes little and the accuracy is high. When the depth exceeds 4 km, the accuracy of the six marine gravity anomaly models and ship-borne gravity data is the worst. The reason for this phenomenon is that the seafloor topography in the deep water area of the study sea area changes dramatically. An analysis was conducted based on the different results and distribution of gravity anomalies retrieved by Grav-3 and ship-borne gravity data when the depth exceeds 4 km, i.e., using the seafloor topography in this area as an example.

It can be seen from Fig. 8 that most of the points with depths greater than 4 km are distributed near the Yucatan Basin and Cayman Trench in the study area, and the seafloor topography in this area changes dramatically. The dramatic changes in seafloor

Table 6. Statistics of differences between marine gravity anomaly models and the ship-borne gravity data measured values at different depths

Model	Depth/km	Data number	Max/mGal	Min/mGal	Mean/mGal	STD/mGal	RMS/mGal
Grav-1	<1	93 723	24.69	−34.73	−0.29	3.33	3.34
	1–2	48 005	37.81	−36.17	0.07	4.31	4.31
	2–3	37 387	38.53	−33.80	−0.44	3.87	3.89
	3–4	56 472	34.80	−35.78	−0.35	3.22	3.23
	>4	14 321	37.72	−33.56	0.43	4.92	4.94
Grav-2	<1	93 723	24.71	−37.64	−0.26	3.35	3.36
	1–2	48 005	37.88	−36.16	0.09	4.31	4.31
	2–3	37 387	38.49	−33.86	0.43	3.87	3.90
	3–4	56 472	34.74	−35.77	0.35	3.22	3.24
	>4	14 321	37.73	−33.59	0.42	4.92	4.94
Grav-3	<1	93 723	25.76	−33.05	−0.29	3.25	3.26
	1–2	48 005	37.91	−35.81	0.08	4.24	4.24
	2–3	37 387	39.31	−33.36	0.43	3.83	3.86
	3–4	56 472	35.85	−35.62	0.35	3.20	3.22
	>4	14 321	37.33	−33.82	0.42	4.91	4.93
Grav-4	<1	93 723	25.80	−33.07	−0.26	3.25	3.26
	1–2	48 005	37.99	−35.79	0.09	4.25	4.25
	2–3	37 387	39.30	−33.46	0.41	3.84	3.86
	3–4	56 472	35.80	−35.61	0.35	3.21	3.23
	>4	14 321	37.37	−33.86	0.41	4.91	4.92
Grav-5	<1	93 723	23.99	−35.74	−0.30	3.30	3.32
	1–2	48 005	38.12	−35.97	0.06	4.47	4.47
	2–3	37 387	38.19	−34.07	0.44	3.95	3.97
	3–4	56 472	36.29	−35.31	0.35	3.25	3.27
	>4	14 321	37.69	−34.41	0.48	5.02	5.04
Grav-6	<1	93 723	24.04	−35.51	−0.25	3.29	3.30
	1–2	48 005	38.17	−35.94	0.11	4.47	4.47
	2–3	37 387	38.20	−34.09	0.43	3.95	3.97
	3–4	56 472	36.22	−35.31	0.35	3.25	3.27
	>4	14 321	37.70	−34.44	0.48	5.02	5.04

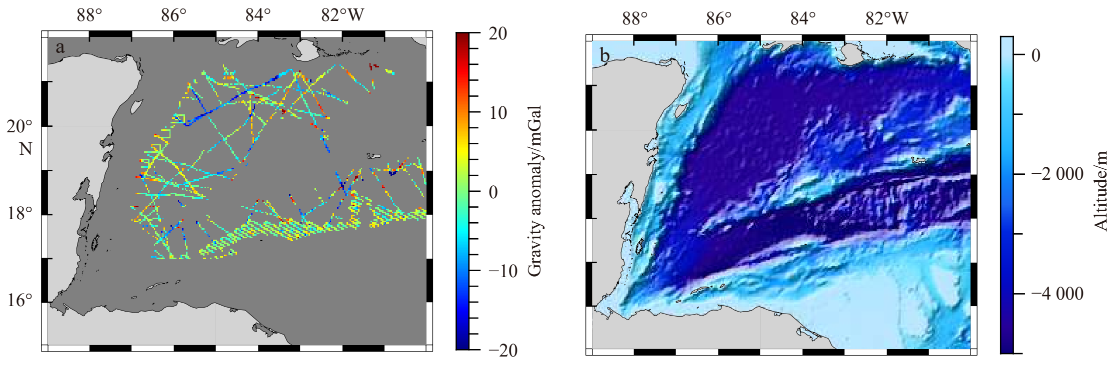

Fig. 8. Distribution of differences between Grav-3 and the ship-borne gravity data at depth >4 km, and seafloor topography in this area. The light gray area is land; the dark gray area represents the marine region.

topography cause dramatic changes in gravity anomalies. Because the derivation of gravity anomalies using the method in this study uses the MSS data within a certain window range, the derivation accuracy is low at the place where the gravity anomaly changes violently.

To further study the influence of seafloor topography changes on the gravity derivation accuracy, using SIO topo_23.1, the east direction component $\mathrm{d}h_x$ and north direction component $\mathrm{d}h_y$ of the seafloor topographic gradient in the study sea area are calculated. The seafloor topographic gradient $\mathrm{d}h$ at the grid point can be obtained as follows:

$$\mathrm{d}h = \sqrt{\mathrm{d}h_x^2 + \mathrm{d}h_y^2}. \tag{9}$$

It can be seen from Table 7 that, in the range of seafloor topography gradient from 0 arcmin to 250 arcmin, with the increase of the seafloor topography gradient, the difference between the gravity anomaly retrieved from the MSS model and ship-borne gravity data will also increase. Owing to the drastic changes in the seafloor topography, the gravity anomalies change dramatically, so the derivation accuracy is correspondingly low.

5 Conclusions

In this study, the removal-recovery method, MSS model, MDT model, and XGM2019e_2159 gravity field model are combined, and the IVM formula is used to invert gravity anomalies in the Gulf of Mexico. The accuracy of the marine gravity anomalies as determined from the MSS model is comprehensively evaluated. The following conclusions can be drawn.

(1) The accuracy of the difference between the gravity anomalies derived by DTU21MSS and CNES_CLS18MDT and the ship-borne gravity data is optimal.

(2) The gravity anomalies of the six marine gravity anomaly models at different coastal distances are compared and analyzed with the ship-borne gravity data. With the increase of the distance from the coast, the RMS of the difference between the six marine gravity anomaly models and ship-borne gravity data gradually decreases.

(3) The gravity anomalies of the six marine gravity anomaly

Table 7. Statistics of differences between marine gravity anomaly models and the ship-borne gravity data at different submarine topography gradients

Model	Seafloor topographic gradient/(m·arcmin^{-1})	Data number	Max/mGal	Min/mGal	Mean/mGal	STD/mGal	RMS/mGal
Grav-1	<50	182 668	37.81	−35.78	0.07	3.25	3.25
	50–100	28 246	37.29	−31.79	−0.03	4.14	4.14
	100–150	14 099	34.07	−33.25	0.07	4.57	4.57
	150–200	7 893	37.72	−33.56	0.18	4.74	4.74
	200–250	5 060	35.58	−30.24	0.06	4.93	4.93
	>250	11 925	38.53	−36.17	0.30	6.01	6.01
Grav-2	<50	182 668	37.88	−35.77	0.09	3.25	3.25
	50–100	28 246	37.29	−37.60	−0.03	4.15	4.15
	100–150	14 099	34.01	−37.64	0.04	4.66	4.66
	150–200	7 893	37.73	−33.59	0.19	4.75	4.75
	200–250	5 060	35.54	−30.61	0.04	4.99	4.99
	>250	11 925	38.49	−36.16	0.32	6.01	6.02
Grav-3	<50	182 668	37.91	−35.62	0.06	3.22	3.22
	50–100	28 246	36.85	−31.76	−0.02	4.06	4.06
	100–150	14 099	34.82	−34.04	0.11	4.40	4.40
	150–200	7 893	37.33	−33.82	0.18	4.67	4.67
	200–250	5 060	35.55	−30.20	0.05	4.93	4.93
	>250	11 925	39.31	−35.81	0.32	5.93	5.93
Grav-4	<50	182 668	37.99	−35.61	0.08	3.22	3.22
	50–100	28 246	36.88	−31.98	−0.03	4.07	4.07
	100–150	14 099	34.79	−34.06	0.07	4.45	4.45
	150–200	7 893	37.37	−33.86	0.18	4.68	4.68
	200–250	5 060	35.58	−30.24	0.06	4.93	4.93
	>250	11 925	39.30	−35.79	0.33	5.93	5.94
Grav-5	<50	182 668	38.12	−35.74	0.06	3.27	3.28
	50–100	28 246	36.99	−31.05	−0.02	4.24	4.24
	100–150	14 099	33.17	−33.38	0.14	4.58	4.59
	150–200	7 893	37.69	−34.41	0.18	4.89	4.89
	200–250	5 060	35.95	−30.33	0.04	5.14	5.14
	>250	11 925	38.19	−35.97	0.30	6.20	6.21
Grav-6	<50	182 668	38.17	−35.51	0.09	3.27	3.27
	50–100	28 246	36.98	−31.32	−0.01	4.24	4.24
	100–150	14 099	33.17	−33.48	0.13	4.59	4.59
	150–200	7 893	37.70	−34.44	0.21	4.90	4.90
	200–250	5 060	36.04	−30.34	0.07	5.14	5.14
	>250	11 925	38.20	−35.94	0.33	6.20	6.21

models at different depths are compared and analyzed with the ship-borne gravity data. With the increase of water depth, the RMS variation trend of the difference between the six marine gravity anomaly models and ship-borne gravity data is consistent. When the water depth is 3–4 km, the accuracy of the difference between the gravity anomaly retrieved from the MSS model and ship-borne gravity data is optimal. When the water depth exceeds 4 km, the accuracy of the difference between the gravity anomaly retrieved from the MSS model and ship-borne gravity data is the worst. The reason for this phenomenon is that the seafloor topography in the deep water of this sea area changes dramatically.

The above results show that the gravity anomaly derivation in the Gulf of Mexico using the MSS models CNES_CLS15MSS, DTU21MSS, and SDUST2020MSS combined with the MDT models CNES_CLS18MDT and DTU22MDT has high accuracy. It can accurately and effectively invert gravity anomaly distributions in the Gulf of Mexico.

Acknowledgements

We are very grateful to CNES, Technical University of Denmark (DTU) and Shandong University of Science and Technology (SDUST) for providing the MSS models and MDT models, and NCEI for providing the ship-borne gravimetric data. We thank ICGEM for providing the XGM2019e_2159 model, and SIO for providing the seafloor topography model.

References

Andersen O B, Abulaitijiang A, Zhang Shengjun, et al. 2021. A new high resolution mean sea surface (DTU21MSS) for improved sea level monitoring. In: Proceedings of EGU General Assembly 2021. Vienna: EGU, doi: 10.5194/egusphere-egu21-16084

Andersen O B, Knudsen P, Berry P A M. 2010. The DNSC08GRA global marine gravity field from double retracked satellite altimetry. Journal of Geodesy, 84(3): 191–199, doi: 10.1007/s00190-009-0355-9

Andersen O B, Vest A L, Knudsen P. 2005. The KMS04 multi-mission mean sea surface. In: Proceedings of Workshop: GOCINA: Improving Modelling of Ocean Transport and Climate Prediction in the North Atlantic Region Using GOCE Gravimetry. Novotel, Luxembourg: Centre European de Geodynamique et de Seimologie

Chelton D B, Walsh E J, MacArthur J L. 1989. Pulse compression and sea level tracking in satellite altimetry. Journal of Atmospheric and Oceanic Technology, 6(3): 407–438, doi: 10.1175/1520-0426(1989)006<0407:PCASLT>2.0.CO;2

Fairhead J D, Green C M, Odegard M E. 2001. Satellite-derived gravity having an impact on marine exploration. The Leading Edge, 20(8): 873–876, doi: 10.1190/1.1487298

Fu L L, Cazenave A. 2001. Satellite Altimetry and Earth Sciences: A Handbook of Techniques and Applications. San Diego: Academic Press

Gopalapillai S. 1974. Non-global recovery of gravity anomalies from a combination of terrestrial and satellite altimetry data. Columbus: Ohio State University

Gozzard S, Kusznir N, Franke D, et al. 2019. South China Sea crustal thickness and oceanic lithosphere distribution from satellite gravity inversion. Petroleum Geoscience, 25(1): 112–128, doi: 10.1144/petgeo2016-162

Guo Jinyun, Chang Xiaotao, Hwang C, et al. 2010. Oceanic surface geostrophic velocities determined with satellite altimetric crossover method. Chinese Journal of Geophysics, 53(6): 926–934, doi: 10.1002/cjg2.1563

Guo Jinyun, Luo Hongxin, Zhu Chengcheng, et al. 2022. Accuracy comparison of marine gravity derived from HY-2A/GM and CryoSat-2 altimetry data: a case study in the Gulf of Mexico. Geophysical Journal International, 230(2): 1267–1279, doi: 10.1093/gji/ggac114

Hwang C. 1998. Inverse Vening Meinesz formula and deflection-geoid formula: applications to the predictions of gravity and geoid over the South China Sea. Journal of Geodesy, 72(5): 304–312, doi: 10.1007/s001900050169

Hwang C, Chang E T Y. 2014. Seafloor secrets revealed. Science, 346: 32–33, doi: 10.1126/science.1260459

Hwang C, Parsons B. 1995. Gravity anomalies derived from Seasat, Geosat, ERS-1 and TOPEX/POSEIDON altimetry and ship gravity: a case study over the Reykjanes Ridge. Geophysical Journal International, 122(2): 551–568, doi: 10.1111/j.1365-246X.1995.tb07013.x

Ismael M. 2014. Tectonostratigraphic stages in the Mesozoic opening and subsidence of the Gulf of Mexico based on deep-penetration seismic reflection data in the salt-free eastern part of the basin [dissertation]. Houston: University of Houston

Jin Taoyong, Li Jiancheng. 2012. Calibration of the linear drift of mean sea level change from satellite altimetry using tide gauge observations. Geomatics and Information Science of Wuhan University (in Chinese), 37(10): 1194–1197, doi: 10.13203/j.whugis2012.10.020

Li Zhen, Guo Jinyun, Ji Bing, et al. 2022a. A review of marine gravity field recovery from satellite altimetry. Remote Sensing, 14(19): 4790, doi: 10.3390/rs14194790

Li Yang, Guo Jinyun, Sun Yu, et al. 2022b. Inversion of global sea level change and its component contributions by combining time-varying gravity data and altimetry data. Acta Geodaetica et Cartographica Sinica, 51(8): 1768–1778, doi: 10.11947/j.AGCS.2022.20210169

Liu Liang, Jiang Xiaoguang, Liu Shanwei, et al. 2016. Calculating the marine gravity anomaly of the South China Sea based on the inverse stokes formula. IOP Conference Series: Earth and Environmental Science, 46: 012062, doi: 10.1088/1755-1315/46/1/012062

Mulet S, Rio M H, Etienne H, et al. 2021. The new CNES-CLS18 global mean dynamic topography. Ocean Science, 17(3): 789–808, doi: 10.5194/os-17-789-2021

Pujol M I, Schaeffer P, Faugère Y, et al. 2018. Gauging the improvement of recent mean sea surface models: a new approach for identifying and quantifying their errors. Journal of Geophysical Research: Oceans, 123(8): 5889–5911, doi: 10.1029/2017JC013503

Rapp R H. 1979. Geos 3 data processing for the recovery of geoid undulations and gravity anomalies. Journal of Geophysical Research: Solid Earth, 84(B8): 3784–3792, doi: 10.1029/JB084iB08p03784

Sandwell D, Garcia E, Soofi K, et al. 2013. Toward 1-mGal accuracy in global marine gravity from CryoSat-2, Envisat, and Jason-1. The Leading Edge, 32(8): 892–899, doi: 10.1190/tle32080892.1

Sandwell D T, Müller R D, Smith W H F, et al. 2014. New global marine gravity model from CryoSat-2 and Jason-1 reveals buried tectonic structure. Science, 346(6205): 65–67, doi: 10.1126/science.1258213

Sandwell D T, Smith W H F. 1997. Marine gravity anomaly from Geosat and ERS 1 satellite altimetry. Journal of Geophysical Research: Solid Earth, 102(B5): 10039–10054, doi: 10.1029/96jb03223

Smith G N. 1974. Mean gravity anomaly prediction from terrestrial gravity data and satellite altimetry data [dissertation]. Columbus: The Ohio State University Columbus

Stanev E V, Peneva E L. 2001. Regional sea level response to global climatic change: Black Sea examples. Global and Planetary Change, 32(1): 33–47, doi: 10.1016/S0921-8181(01)00148-5

Wan Xiaoyun, Yu Jinhai. 2013. Mean dynamic topography calculated by GOCE gravity field model and CNES-CLS2010 mean sea surface height. Chinese Journal of Geophysics (in Chinese), 56(6): 1850–1856, doi: 10.6038/cjg20130607

Yang Junjun, Jekeli C, Liu Lintao. 2018. Seafloor topography estimation from gravity gradients using simulated annealing. Journal of Geophysical Research: Solid Earth, 123(8): 6958–6975, doi: 10.1029/2018jb015883

Yuan Jiajia, Guo Jinyun, Zhu Chengcheng, et al. 2021. High-resolution sea level change around China seas revealed through multi-satellite altimeter data. International Journal of Applied Earth Observation and Geoinformation, 102: 102433, doi: 10.1016/j.jag.2021.102433

Yuan Jiajia, Guo Jinyun, Zhu Chengcheng, et al. 2023. SDUST2020 MSS: A global 1′ × 1′ mean sea surface model determined from multi-satellite altimetry data. Earth System Science Data, 15(1): 155–169, doi: 10.5194/essd-15-155-2023

Zaron E D. 2019. Simultaneous estimation of ocean tides and underwater topography in the Weddell Sea. Journal of Geophysical Research: Oceans, 124(5): 3125–3148, doi: 10.1029/2019JC015037

Zhu Chengcheng, Guo Jinyun, Hwang C, et al. 2019. How HY-2A/GM altimeter performs in marine gravity derivation: assessment in the South China Sea. Geophysical Journal International, 219(2): 1056–1064, doi: 10.1093/gji/ggz330

Zhu Chengcheng, Guo Jinyun, Yuan Jiajia, et al. 2021. Refining altimeter-derived gravity anomaly model from shipborne gravity by multi-layer perceptron neural network: a case in the South China Sea. Remote Sensing, 13(4): 607, doi: 10.3390/rs13040607

Zhu Chengcheng, Guo Jinyun, Yuan Jiajia, et al. 2022. SDUST 2021GRA: Global marine gravity anomaly model recovered from Ka-band and Ku-band satellite altimeter data. Earth System Science Data, 14(10): 4589–4606, doi: 10.5194/essd-14-4589-2022

Zingerle P, Pail R, Gruber T, et al. 2020. The combined global gravity field model XGM2019e. Journal of Geodesy, 94(7): 66, doi: 10.1007/s00190-020-01398-0